



Article

Nitrogen-Related High-Spin Vacancy Defects in Bulk (SiC) and 2D (hBN) Crystals: Comparative Magnetic Resonance (EPR and ENDOR) Study

Larisa Latypova^{1,2}, Fadis Murzakhanov^{3,*} , George Mamin³, Margarita Sadovnikova³, Hans Jurgen von Bardeleben⁴ and Marat Gafurov³ 

- ¹ School of Chemistry and Chemical Engineering, Harbin Institute of Technology, 92 West Da-Zhi Street, Harbin 150001, China; larisa.latypova@hit.edu.cn
- ² Zhengzhou Research Institute, Harbin Institute of Technology, 26 Intersection of Longyuan East 7th Street and Longhu Central North Road, Zhengdong New District, Zhengzhou 450000, China
- ³ Institute of Physics, Kazan Federal University, Kremlevskaya 18, 420008 Kazan, Russia; georgemamin@gmail.com (G.M.); margaritaasadov@gmail.com (M.S.); mgafurov@gmail.com (M.G.)
- ⁴ Institut des Nanosciences de Paris, Sorbonne Université, Campus Pierre et Marie Curie, 4, Place Jussieu, 75005 Paris, France; vonbarde@insp.jussieu.fr
- * Correspondence: murzakhanov.fadis@yandex.ru; Tel.: +7-(843)-2926480

Abstract: The distinct spin, optical, and coherence characteristics of solid-state spin defects in semiconductors have positioned them as potential qubits for quantum technologies. Both bulk and two-dimensional materials, with varying structural properties, can serve as crystalline hosts for color centers. In this study, we conduct a comparative analysis of the spin–optical, electron–nuclear, and relaxation properties of nitrogen-bound vacancy defects using electron paramagnetic resonance (EPR) and electron–nuclear double resonance (ENDOR) techniques. We examine key parameters of the spin Hamiltonian for the nitrogen vacancy (NV^-) center in 4H-SiC: $D = 1.3$ GHz, $A_{zz} = 1.1$ MHz, and $C_Q = 2.53$ MHz, as well as for the boron vacancy (V_B^-) in hBN: $D = 3.6$ GHz, $A_{zz} = 85$ MHz, and $C_Q = 2.11$ MHz, and their dependence on the material matrix. The spin–spin relaxation times T_2 (NV^- center: 50 μ s and V_B^- : 15 μ s) are influenced by the local nuclear environment and spin diffusion while Rabi oscillation damping times depend on crystal size and the spatial distribution of microwave excitation. The ENDOR absorption width varies significantly among color centers due to differences in crystal structures. These findings underscore the importance of selecting an appropriate material platform for developing quantum registers based on high-spin color centers in quantum information systems.

Keywords: color centers; semiconductors; electron paramagnetic resonance; NV^- center; boron vacancy; silicon carbide; hexagonal boron nitride



Citation: Latypova, L.; Murzakhanov, F.; Mamin, G.; Sadovnikova, M.; von Bardeleben, H.J.; Gafurov, M. Nitrogen-Related High-Spin Vacancy Defects in Bulk (SiC) and 2D (hBN) Crystals: Comparative Magnetic Resonance (EPR and ENDOR) Study. *Quantum Rep.* **2024**, *6*, 263–277. <https://doi.org/10.3390/quantum6020019>

Academic Editor: Yanpeng Zhang

Received: 3 May 2024

Revised: 12 June 2024

Accepted: 12 June 2024

Published: 14 June 2024



Copyright: © 2024 by the authors. Licensee MDPI, Basel, Switzerland. This article is an open access article distributed under the terms and conditions of the Creative Commons Attribution (CC BY) license (<https://creativecommons.org/licenses/by/4.0/>).

1. Introduction

Over the past decades, spin defects in solids have attracted countless interests in rapidly advancing quantum technologies due to their promising applications in computing, communication, and sensing [1–4]. The combination of optical, coherent, and charge properties of point defects, called color centers, predetermined their scientific and technological development and study by a wide range of experimental techniques [5]. Based on the well-known nitrogen vacancy (NV^-) centers in diamond [6], long-lived quantum entanglement has been demonstrated, many quantum algorithms for performing logical operations and quantum cryptography have been implemented, and finally prototypes of nano-scale temperature and magnetic field sensors have been shown [7]. The modification adaptability of the NV^- center and superconducting qubits has led to the design of solid-state hybrid quantum systems that are more resistant to a decoherence with significantly increased

mutual coupling strength [8]. A high-fidelity implementation of hybrid gates can offer an attractive way of quantum information processing and robust quantum state transfer [9].

Despite the existing scientific work on quantum superiority in relation to classical computers [10], all advances based on qubits, implemented not only on color centers, but also using ultracold atoms, trapped ions, and superconducting contacts, are still at the level of simulation calculations for highly targeted specialized tasks. Competitive similar platforms have the following disadvantages: (i) superconducting qubits—substrate dielectric loss and excess quasiparticles in superconducting metal cause dissipation and dephasing; (ii) gate-defined quantum dots—charge traps and magnetic impurities at the dielectric interfaces or interface inhomogeneity (variation in valley splitting and spin–orbit coupling) can destroy the evolution of the quantum state; (iii) ion traps—electric-field noise heats ion motion; and (iv) Majorana zero modes—defect density in nanowires and semiconductor–superconductor nanowire interfaces that creates a proximity hard gap [11]. Contemporaneously, spin defects are technically easily created, both ensembles and single centers, detected at room temperature using a wide range of methods, and integrated into existing semiconductor technology. High-spin defect in semiconductor materials has been qualitatively tested and confirmed many times as a reliable quantum bit (qubit) [2–4]. Thus, the search and development of new promising materials with a sequence of qubits continues, capable of bringing quantum information technologies to a new level of universal computing for a wide range of multidisciplinary practical problems.

With semiconductor structures similar to diamonds, covalent bulk crystals of silicon carbide (SiC) are increasingly mentioned and used, having a diverse polytype structure that is resistant to mechanical, temperature, and radiation influences [12]. The wide-gap semiconductor SiC can act as a base matrix for high-spin ($S = 1$ and $S = 3/2$) color centers of the most diverse nature (structure). Thus, using magnetic resonance spectroscopy methods over a wide temperature range, silicon vacancies (V_{Si}) [12,13] and divacancies (VV) [14] have been discovered in various SiC crystal polytypes (3C, 4H, 6H, and 15R), demonstrating unique spin–optical properties and long millisecond relaxation times. Most importantly, in SiC impurity crystals with nitrogen atoms, NV^- centers have been identified, which have a direct microscopic structure similar to color centers in diamond [15,16]. The mentioned color centers are photoactive defects, where optical excitation leads to effective spin polarization with the formation of subsequent population inversion. In addition to the higher manufacturability and lower cost of obtaining a crystal compared to diamond, color centers in SiC have an intense luminescence signal in the infrared (IR) range with wavelengths of 1.1–1.2 μm (in diamond 640 nm), which corresponds to the transmission band of biological tissues and fiber optic information transmission networks [17,18]. Thus, high-spin defects in SiC have high potential for practical applicability in the biomedical field as quantum sensors and communications, where the SiC crystal can be quite easily integrated into existing semiconductor electronics, including high-power devices [19].

In addition to bulk crystals, a new completely different type of crystalline matrix has been proposed—two-dimensional materials, which usually have strong sp^2 -hybridized covalent bonds, within the layer and weak van der Waals bonds between the layers [20]. The increasingly popular hexagonal boron nitride (hBN) is a wide-gap direct semiconductor (6 eV) and isoelectronic analogue of graphene, with the same interlayer distance of about 3.3 Å [21]. hBN crystal can contain both intrinsic and artificially induced defects with electron spin $S = 1$, where the nature of a boron vacancy (V_B^-) with point symmetry D_{6h} surrounded by three equivalent nitrogen atoms has been established using microwave spectroscopy [22]. The luminescence spectrum of a V_B^- has a wavelength of 780 nm when optically pumped from the ground to the excited state by visible light with $\lambda = 532$ nm. The electron spin of a V_B^- has also been proposed as a qubit, which has proven itself to a greater extent as a basis for temperature and pressure sensors due to the high “flexibility” and sensitivity of the structure to external influences and as a single-photon source [23,24]. It has also been established that the spin properties of a V_B^- in hBN do not depend on the number of BN layers of the crystal and are determined by the local environment of the

defect [25]. In theory, by delaminating hBN, one can move to the monoatomic limiting state of the condensed state of the material with the possibility of creating angstrom-scale quantum sensors based on a boron vacancy. The fundamental difference from the SiC crystal, in addition to the dimensions, is the extremely concentrated nuclear spin bath with isotopes of boron (^{10}B , $I = 3/2$, 19.9% and ^{11}B , $I = 1$, 80.1%) and nitrogen (^{14}N , $I = 1$, 99.69%). In addition, SiC is a practically non-magnetic crystal containing ^{13}C ($I = 1/2$ and 1.13%) and ^{29}Si ($I = 1/2$, 15%), which affects the relaxation properties of color centers.

New platforms in the form of SiC and hBN are extremely promising materials, large-scale studies of the unique properties and features of which are still ongoing. Stable defects in these compounds are easily created by electron, proton, and neutron irradiation with high-energy particles (≥ 1 MeV), as well as using a femtosecond laser and ion implantation [26,27]. In this case, irradiation with nominal absorption doses of 10^{17} – 10^{18} cm^{-2} leads to a uniform distribution of point defects within the crystal without cluster formation with destruction of the crystal structure. It has been shown that these centers are temperature stable (color centers up to 2000 °C) and do not disappear (recombine) over time [28]. Despite preliminary exposure in the form of intense irradiation of crystals and the introduction of various impurities during crystal growth, the materials retain their high quality and degree of crystallinity, which is extremely important for the ensemble system of defects from a spectroscopic point of view [26].

Electron paramagnetic resonance (EPR) is the most suitable method for detecting, identifying, and studying the spin properties of color centers in semiconductors. The use of pulse sequences allows manipulation of spin magnetization and determination of phase coherence time (T_2). Combined with optical excitation and double resonance using an additional radiofrequency (RF) source to initiate nuclear magnetic resonance (NMR) transitions, this technique is a powerful spectroscopic tool for determining the microscopic structure of the color center and the features of the electron–nuclear interaction of the defect with the local environment.

The novelty of the current scientific work lies in the study of color centers by various EPR-based techniques at the high frequency (W-band, 94 GHz), complementing the classical X-band (9.4 GHz) measurements. The transition to the high-frequency range with a corresponding increase in the magnetic field by 10 times makes it possible to significantly increase the sensitivity and spectroscopic resolution of EPR detection. Simultaneously, a high magnetic field (3.4 T) provides pure spin wave functions through a Zeeman interaction term in contrast to optically detected magnetic resonance (ODMR) spectroscopy with low field measurements (10–20 mT). The application of EPR with various pulse sequences makes it possible to obtain information about the dynamic (relaxation) characteristics of color centers and to explore spin manipulability properties by Rabi oscillations. The use of photoinduced EPR and electron–nuclear double resonance (ENDOR) spectroscopy with multipulse sequences, encompassing optical, microwave, and radio frequency resonant transitions, facilitates a comprehensive investigation of studied color centers as robust combined qubits for quantum technologies. The main novelty lies in the first comparative analysis of the spin–optical and coherence properties of vacancy defects structurally related to nitrogen as an NV^- center in diamond, but localized in two fundamentally different systems (2D (van der Waals material), magnetically saturated—hBN and 3D (bulk), magnetically dilute—SiC).

In this work, using EPR and ENDOR spectroscopies, the fundamental spectroscopic differences are shown for spin defects ($S = 1$) of the vacancy type associated with nitrogen atoms, and namely the NV^- center in SiC (3D, magnetically diluted) and the V_B^- boron vacancy in hBN (2D, magnetically saturated system), coordinated over three equivalent nitrogen atoms. The difference in the magnitude of the splitting in a zero magnetic field D , in hyperfine A and quadrupole Q interactions, as well as in the times of spin–spin and spin–lattice relaxations together with Rabi oscillations has been demonstrated.

2. Materials and Methods

The 4H-SiC sample studied in this work was a commercial N-doped ($2 \times 10^{17} \text{ cm}^{-3}$) n-type 4H-SiC single crystal. It had been irradiated at $Temp. = 295 \text{ K}$ with 12 MeV protons at a total fluence of $1 \times 10^{16} \text{ cm}^{-2}$ in order to create Si vacancy centers. The sample was then annealed at a temperature $Temp. = 900 \text{ }^\circ\text{C}$, to allow the formation of $V_{\text{Si}}N_{\text{C}}$ complexes by Si vacancy diffusion. A typical sample size was $0.8 \text{ mm} \times 0.4 \text{ mm} \times 0.2 \text{ mm}$. Figure 1a–c illustrate the sample mounting for the magnetic resonance measurements.

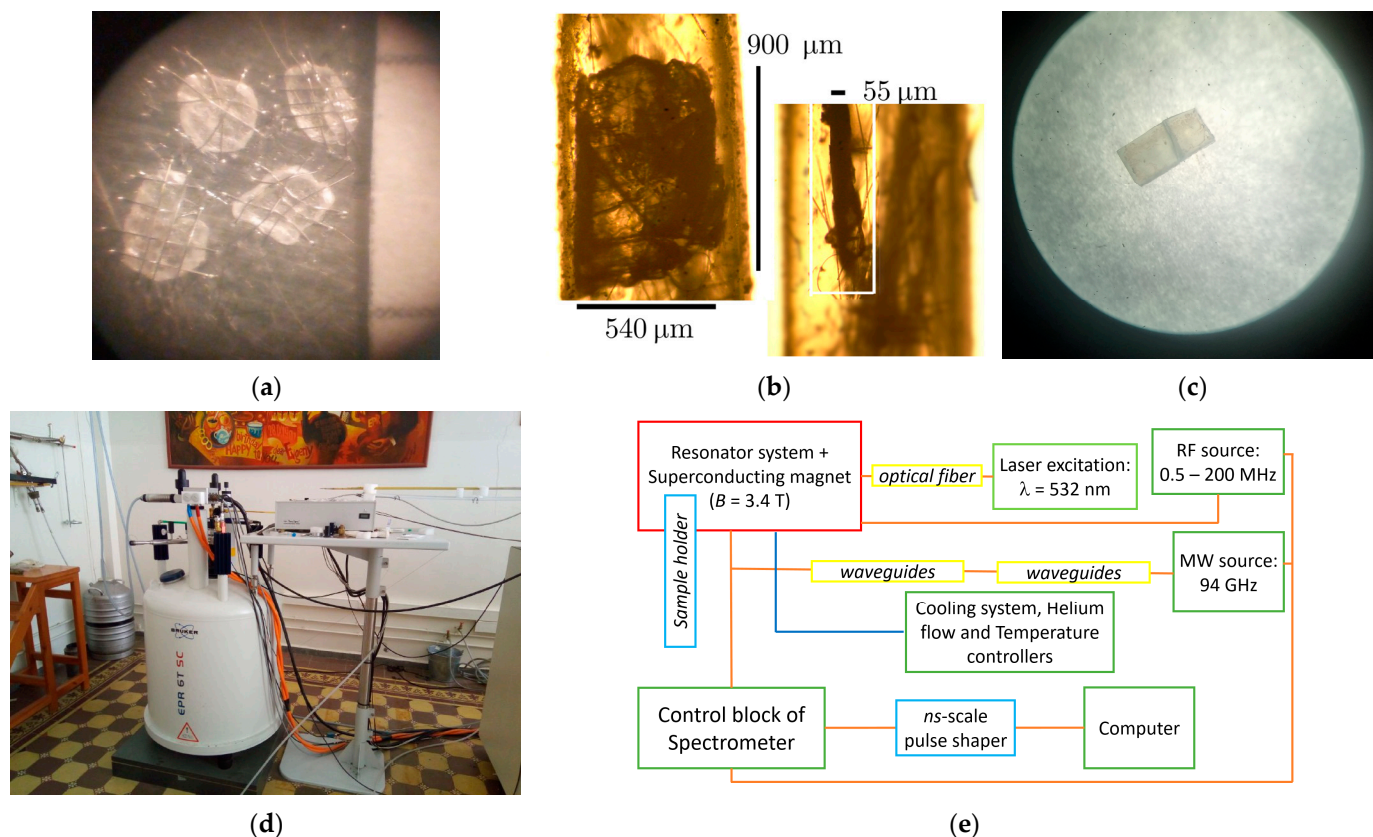


Figure 1. (a) hBN crystals mounted on an aluminum substrate before electron irradiation. The distance between the black horizontal lines on the right is 5 mm; (b) Samples under study prepared for high-frequency part of the spectrometer. The characteristic dimensions of the samples and capillaries correspond to the internal diameter of the resonator to achieve the highest filling factor; (c) Bulk crystal ($0.42 \times 0.67 \times 1.22 \text{ mm}^3$) of silicon carbide under an optical microscope during the preparation of samples for experiments; (d) Bruker Elexsys E680 spectrometer operating at 94 GHz (W-band) equipped with helium flow cryostat; (e) Measurement setup diagram including the main blocks of the spectrometer for the photoinduced EPR and ENDOR.

The hBN single crystals with dimensions of $900 \text{ } \mu\text{m} \times 540 \text{ } \mu\text{m} \times 55 \text{ } \mu\text{m}$ used in this study were commercially produced by the HQ Graphene company. The samples were irradiated at room temperature with 2 MeV electrons to a total dose of $6 \times 10^{18} \text{ cm}^{-2}$. No annealing treatments were applied to the irradiated samples.

The magnetic resonance experiments were carried out with a W-band Bruker Elexsys E680 commercial spectrometer (Bruker, Karlsruhe, Germany, Figure 1d) operated in a pulsed mode. The samples under study were prepared for experiments using an optical microscope, special diamond files, and tweezers to fit the crystals for the resonator cavity. The high-frequency EPR spectrometer was equipped with a cylindrical dielectric resonator with characteristic dimensions of 3 mm, which corresponds to a microwave excitation wavelength of $\nu_{\text{MW}} = 94 \text{ GHz}$. The safe placement of crystals into the resonator cavity was

carried out using a sample holder with a quartz capillary (inner radius of 450 μm). The main spectrometer blocks are presented in Figure 1e.

The EPR spectra were recorded by detecting the amplitude of the primary electron spin echo (ESE) as a function of the magnetic field sweep B using a pulse sequence $\pi/2 - \tau - \pi - \tau - ESE$, where $\pi/2 = 40$ ns and $\tau = 240$ ns. Short nanosecond-scale microwave pulses required a 1 kW amplifier to achieve a 90- or 180-degree spin magnetization rotation in a rotational coordinate system. Pulse sequences were specified and configured using the EasyPanel and Advanced modes, allowing one to accurately optimize the pulse durations, intervals, and integration areas of the electron spin echo in 4 ns steps. To achieve undistorted and saturated EPR signals at each temperature and a distinct color center, the short repetition time (SRT) was continuously adjusted, which directly affected the registration speed of one scan. The relaxation times were measured with standard pulse sequences: the Hahn sequence for recording the phase coherence time T_2 and the inversion-recovery sequence ($\pi - T + dT - \pi/2 - \tau - \pi - \tau - ESE$, where $T = 1.5$ μs and $dT = 1$ μs) for recording the spin-lattice relaxation time T_1 . The ENDOR spectra were obtained utilizing the Mims pulse sequence ($\pi_{\text{MW}}/2 - \tau - \pi_{\text{MW}}/2 - \pi_{\text{RF}} - \pi_{\text{MW}}/2 - \tau - ESE$) with a 150 kW RF generator, where $\pi_{\text{RF}} = 72$ μs . A satisfactory signal-to-noise ratio was ensured by multi-scan recording (1024–4096 scans) of the ENDOR spectrum within a reasonable time frame (30 min–2 h). Low temperature measurements were conducted by using a flow helium cryostat from Oxford Instruments. The EPR and ENDOR spectra in the case of NV^- centers in SiC were obtained at a crystal temperature of 150 K, while for the boron vacancy in hBN at 50 K. The dynamic characteristics of spin defects were studied in the range of 7–10 K in order to reduce the influence of temperature fluctuations on phase coherence. The sample could be photoexcited with a green laser ($\lambda = 532$ nm) with an output power of 200 mW. Photoexcitation of color centers during the experiment occurred using an optical fiber integrated with a leak protected sample holder, allowing optical pumping to be used simultaneously with microwave or radio frequency sources without attenuation.

3. Results

3.1. Photoinduced EPR Spectroscopy

The presence of magnetic and spin-orbit interactions between point defects and external sources of “perturbations” leads to a change in the state energy of spin sublevels. In accordance with the symmetry of the center under study and the values of the electronic and nuclear spin, the state operator in the form of a spin Hamiltonian (1) is used to describe and interpret resonant magnetic transitions. The presence of an electric field gradient V_{ij} leads to the so-called “initial” splitting in zero magnetic field between the levels $M_S = \pm 1$ and $M_S = 0$ with a value of D in MHz. The application of a magnetic field through the Zeeman energy leads to the complete removal of the degeneracy of energy levels and the formation of a triplet spin system. Despite the difference in the symmetry group, both defects (NV^- center and boron vacancy V_B^-) are described by the following spin Hamiltonian:

$$H = \mu_B \left(g_{\parallel} B_z S_z + g_{\parallel} (B_x S_x + g_{\parallel} B_y S_y) \right) + D \left(S_z^2 - \frac{2}{3} \right) + E \left(S_x^2 - S_y^2 \right) + A_{\parallel} S_z I_z + A_{\perp} (S_x I_x + S_y I_y) + P \left(I_z^2 - \frac{2}{3} \right) + \eta \left(I_x^2 - I_y^2 \right), \quad (1)$$

where g is the spectroscopic splitting factor, μ_B is the Bohr magneton, $B_{x,y,z}$ is the projections of magnetic field with scalar B_0 values, D and E are the fine structure values, $S_{x,y,z}$ and $I_{x,y,z}$ are the projections of the electron and nuclear spin, and A and P are the values of hyperfine and quadrupole interactions (η —asymmetry parameter). Subscripts (\parallel and \perp) indicate parallel and perpendicular orientation. Here 1–3 terms reflect electron Zeeman interaction, the 4 and 5 terms describe zero-field splitting, the 6–8 terms describe the hyperfine interaction of the electron spin with the nearest to the vacancy ^{14}N nuclear spins. The last 9 and 10 terms are related to the quadrupole interactions.

The echo-detected EPR spectra of color centers are shown in Figure 2a. The spectrum contains two components of the so-called fine structure between $M_S = +1 \leftrightarrow M_S = 0$ (low-field) and $M_S = -1 \leftrightarrow M_S = 0$ (high-field line with the phase inverted by 180°). Under laser excitation (532 nm), the “inter-combination conversion” mechanism (Figure 2b) leads to predominant population of the $M_S = 0$ state, forming a population inversion with the subsequent observation of a stimulated microwave emission signal (high-field component). The highest optical polarization was established for a wavelength of $\lambda = 532$ nm. Side wavelengths result only in a slight change in the EPR signal magnitudes without phase inversion. Ultraviolet radiation (260 nm) can lead to a change in the charge state ($-1/0$) of the color centers with $S = 0$ (EPR silent). Lasers with 260 nm and 405 nm due to a larger energy quantum (3.06 eV and 4.77 eV) lead to a “transfer” of the center to higher excited orbital levels close to the conduction band, which are outside the optimal optical absorption region of the material. Other diode laser sources in a wide range of wavelengths (260–1064 nm) are outside the absorption band of the color centers under study. Accordingly, there is no effective spin polarization through optical pumping.

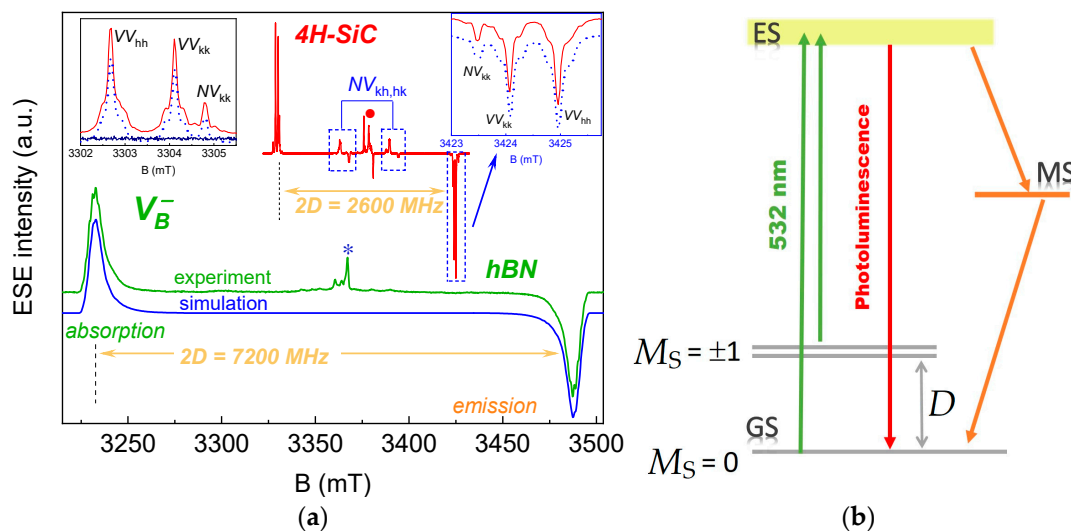


Figure 2. (a) ESE-EPR spectra for an NV^- center in 4H-SiC (top half, red line) and a V_B^- in hBN (bottom half, green line—experiment; blue solid line—simulation). The two insets at top show the detailed recorded low- and high-field components (red solid lines at 532 nm and navy color—“dark” mode) for structurally nonequivalent centers along with the corresponding simulation (blue dashed line). Yellow arrows indicate splittings between the components of the “zero-field splitting”; an asterisk (hBN) and a dot (SiC) indicate optically neutral signals both with spin = $1/2$ from ionic compensators and interstitial defects, respectively, and are outside the scope of our study. (b) Schematic of spin polarization of color centers under optical excitation, where GS is a ground state, ES is an excited state, and MS is a metastable state. D denotes zero-field splitting.

Under the specified experimental parameters, the value of $P = 10$ mW represents the threshold for observing photoinduced EPR spectra. The signal from NV^- centers at $P = 10$ mW is almost comparable to the noise level and only a significantly larger number of experimental data accumulations makes it possible to detect spin defects. A further decrease in power leads to a complete loss of signal from the color centers under study. An increase in laser power also leads to a linear response of NV^- centers in spin polarization. This effect is useful for preliminary “tuning” of qubits, when a certain optical pulse sets its initial state before implementing a quantum algorithm, described by the diagonal elements of the density matrix. With a further increase in P beyond 200 mW, the spin system becomes saturated, leading to exit to the shelf in the intensity of the EPR signal. A negative consequence of using high optical power is local heating of the crystal, which leads to a decrease in electronic relaxation times.

The EPR spectra in Figure 2a are shown in a parallel orientation to the c -axis of the crystal relative (θ —angle between c -axis and B_0) to the external strong magnetic field B_0 , which leads to a $2D$ splitting between the lines due to the angular dependence $D(3\cos^2\theta - 1)$. The main parameters of the spin Hamiltonian (1) for both color centers, obtained by analyzing the EPR spectra, are shown in Table 1. The obtained experimental results obtained are in excellent agreement with previously presented data in pioneering work on the EPR detection of color centers in diamond [6], silicon carbide [29], and hBN [22] crystals. Notable is the difference in the zero-field splitting value of D by almost three times ($3600 \text{ MHz}/1300 \text{ MHz} \approx 2.77$) for defects with the same sign of splitting ($D > 0$) and electron spin $S = 1$ in covalent semiconductors. The «oblate» electron density distribution of a V_B^- has more axial symmetry and is concentrated predominantly in the plane of one BN layer. While the NV^- center in SiC has a «spherical» electron density distribution, dispersed up to several coordination spheres over carbon and silicon. Thus, the two-dimensional structure (nature) of hBN tends to “compress” the electron density between the layers of the crystal and thereby influence the amount of “zero magnetic field splitting”.

Table 1. Parameters of the spin Hamiltonian (1), including the g -factor and the magnitude of splitting in a zero magnetic field. Additionally, a column for the width of EPR lines is shown.

Vacancy Type	$g_{ }$	g_{\perp}	D (MHz)	E (MHz)	EPR Line-Width (MHz)
NV_{kk}^-	2.0065	2.004	1300	0	5
V_B^-	2.0086	2.006	3600	50	37

The EPR spectrum of a SiC crystal can be seen in the inset in Figure 2a, and contains several centers of different nature. Firstly, the presence of two different positions of silicon and carbon (k—quasicubic and h—hexagonal) leads to the formation of two structurally nonequivalent axial NV^- centers, slightly different in spectroscopic values (Table 1 shows data for NV^- in the kk position). The structural features of the crystal lead to a situation where the NV^- center can occupy a position with both axial symmetry and rhombohedral distortion. Color centers with axial symmetry have the point group C_{3v} , and basal ones (kh and hk positions) have lower symmetry with the point group C_{1h} (see top central inset in Figure 2a). The fundamental spectroscopic difference lies in the non-zero E value of the “zero-field splitting” for basal centers, equal to about 50–100 MHz [13]. The axis of the basal NV^- center is declined by 70° relative to the axial NV^- defects directed along the 4H-SiC c -axis. The registration of EPR spectra for basal centers is not optimal, resulting in a lower splitting value (approximately 740 MHz) and poor spectral resolution (upper inset for SiC in the figure, highlighted in a blue square and marked as $NV_{kh,hk}$). The presence of a wide variety of structurally non-equivalent NV^- centers (multiplicity) in a 4H-SiC crystal is an advantage when creating multiqubit quantum registers with subsequent selective excitation and readout of the spin system state. Additionally, upon crystal irradiation and temperature annealing, centers consisting of two paired vacancies of V_{Si} and carbon (V_C), called divacancies, are created, which have already been widely studied by EPR and ODMR spectroscopy. The hBN crystal contains only one type of defect, although centers with different natures (C_N, C_B, V_N) and charge states were previously predicted and found in other studies [30]. The extremely broad appearance of the V_B^- spectrum in hBN is caused by inhomogeneous broadening due to the unresolved hyperfine structure consisting of seven lines. The asymmetric nature of the broadening towards the center of gravity ($g = 2.006$) can be caused either by the delamination of a two-dimensional hBN crystal or the formation of interplanar atomic N-B-N bridges, distorting the local axis of symmetry of the defect [31]. In the case of bulk SiC crystals, the resonance absorption and emission lines are narrow and well spectroscopically resolved, which is important for highly selective excitations in quantum technologies.

3.2. Dynamic Characteristics

The potential suitability of a color center as a qubit is largely determined by the phase coherence time during which a particular pulse sequence can be applied to implement a quantum algorithm. For spin defects in solids, the boundary value of the phase coherence time depends primarily on the degree of spin–spin interaction between the defects and the state of the nuclear spin bath. The dynamic characteristics of paramagnetic centers can be described using two key time parameters: spin–lattice (T_1) and spin–spin (T_2) relaxation times. Spin–lattice (or longitudinal) relaxation is the irreversible spin system evolution toward thermal equilibrium owing to the interaction of an electron spin with phonon vibration modes through spin–orbital coupling. The rate of electronic longitudinal relaxation depends primarily on the crystal temperature and is determined by the Orbach–Aminov mechanisms, one or two-phonon Raman, and “Direct” (dependence on frequency/magnetic field is added) processes. In turn, the spin–spin interaction is responsible for the relaxation of electronic transverse magnetization and depends on the coupling strength as $1/r^3$ (inter-defect distance, r) between two equivalent paramagnetic centers [32]. Spin–spin interaction leads to an irreversible loss of transverse magnetization of the spin packet ensemble due to stochastic changes in the phase of individual centers, therefore T_2 characterizes the so-called phase coherence time. Thus, the spin–lattice relaxation rate characterizes the transfer of energy (thermal) from the spin system to the crystal lattice, while the spin–spin time determines the distribution of the total energy within the electron spin bath, similar to spin diffusion [33]. The presence of several mechanisms or sources of loss of spin magnetization (quantum information) expands the degree of freedom of spatial transfer (propagation) of energy within the crystal. Figure 3 shows the dephasing curves of the amplitude of the electronic magnetization of a defect depending on the type of color center and interaction. In the case of the NV^- center, the relaxation time T_2 is three times longer than that of a V_B^- ($50 \mu\text{s}/15 \mu\text{s} \approx 3.33$), while the overall concentration and degree of uniformity of the distribution of defects within the crystal are the same. The V_B^- surrounded by three magnetic nitrogen nuclei at a distance of 1.4 \AA has a hyperfine electron–nuclear interaction, which, due to local fluctuations in the magnetic field, leads to a loss of phase coherence. The described mechanism relates to nuclear spin diffusion and in the case of a V_B^- in an hBN crystal sets an upper maximum limit of $18 \mu\text{s}$, calculated by cluster calculations [34]. The presence of nuclear spin diffusion manifests itself as a non-exponential (extended) decrease in the transverse magnetization of a V_B^- and the presence of modulations due to the ESEEM effect (electron spin echo envelop modulation). The NV^- center in SiC, in turn, is surrounded by a magnetically dilute medium and the T_2 curve is described by a single exponential without the manifestation of nuclear modulations.

In Figure 3, for each center, Rabi oscillations are shown, the meaning of which is the rotation of the spin magnetization around one of the axes (x or y) in a rotating coordinate system by a long pulse. The registration of Rabi oscillations is a qualitative demonstration of a spin defect acting as an electron qubit, since this experiment allows for “quantum manipulation”, which is one of the criteria for qubits. The Rabi oscillation damping time τ_R more closely reflects the duration of the evolution of spin magnetization, at which quantum protocols can be applied in the form of multi-pulse sequences. In the simple case, one rotation of 180 degrees (π -pulse) corresponds to the quantum operation “NOT”, similar to the classical version. In the case of a V_B^- , the decay is more monotonic and is twice as long as for an NV^- center. It has been established that in such systems the main dephasing mechanism is the insufficient distribution of the magnetic component B_1 in the spectrometer cavity, which leads to a spread in the electronic Larmor frequencies Ω .

Neglecting millisecond-scale spin–lattice relaxation, Rabi damping mechanisms can be handled by taking into account the interaction of the defect center with the neighboring spins, divided into two groups:

- (i) non-resonant spins whose Larmor frequencies differ from ω_0 (nuclei, as well as other spin defects);
- (ii) neighboring V_B^- centers.

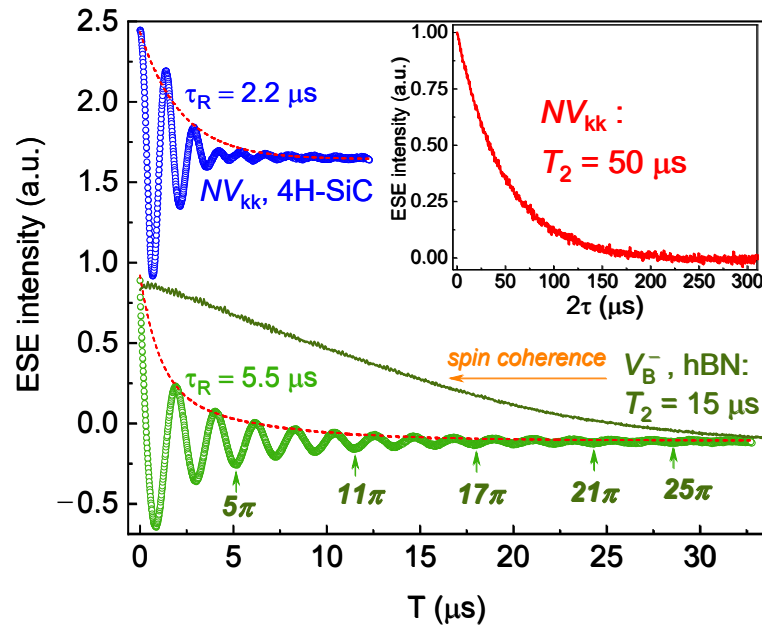


Figure 3. Dynamic characteristics of color centers obtained at $Temp. = 10$ K and optical excitation with $\lambda = 532$ nm. The upper part shows the curves of Rabi oscillations (blue dots) and transverse relaxation time (red solid line in the inset) for NV^- centers in SiC, and for V_B^- in hBN (Rabi oscillations are shown as green dots, transverse relaxations are shown as a solid dark green line). Red dashed lines for each center show decay traces of Rabi oscillations with characteristic damping time τ_R .

Under the application of the driving microwave pulse, the magnetization of a single spin packet detuned from resonance by $\varepsilon = \omega - \omega_0$ rotates with frequency $\Omega = \sqrt{\Omega_R^2 + \varepsilon^2}$. Apart from the spectral inhomogeneity of Ω , one should also take into account the spatial inhomogeneity $\Omega_R(r)$ that originates from the intrinsic distribution of the B_1 field in the resonator. Since the concentration of the spin defects of other types is assumed to be low, the most relevant types of (i) are the magnetic nuclei ^{10}B , ^{11}B , and ^{14}N . In the absence of resonant electron–nuclear cross-relaxation (occurring when Ω_R is close to the nuclear Larmor frequency), the remaining relaxation pathway is due to the second-order process of dephasing in the rotation reference frame of the electron spin, which is limited by the rate of the nuclear bath internal dynamics (governed by the nuclear spin diffusion). Because of the second-order contribution of hyperfine interaction to $\sqrt{\Omega_R^2 + \varepsilon^2}$ via small random shifts of ε , the resulting damping rate of Rabi oscillations is much smaller than the corresponding phase relaxation rate T_2^{-1} that results directly from fluctuations of ε .

As for (ii), we take into account the dipolar interactions with the color centers using the microscopic model for damping rate which is valid in the particular case of small defect concentration:

$$\tau_R^{-1} = \Delta\omega_d \Omega_R \frac{\Omega_R^2 \cos \Omega t}{\Omega^2} \log \frac{2\sigma}{\Omega_R} \quad (2)$$

where $\Delta\omega_d = 4\pi^2 g_e^2 \mu_B^2 C / (9\sqrt{3}\hbar)$ is the dipolar half-width of the resonance line, and $\Omega_R \ll \sigma$ (Rabi frequency much less than the inhomogeneous line half-width). For the estimated concentration of defects $C \approx 6 \times 10^{17} \text{ cm}^{-3}$, one obtains $\Delta\omega_d = 5 \times 10^5 \text{ rad/s}$. The value of τ_R^{-1} depends on spatial inhomogeneity $\Omega_R(r)$ and, correspondingly, crystal size covering this resonance-off area [35].

Spin–lattice relaxation at 10 K has little effect on the phase coherence of the defect (<10%) since the time T_1 is usually one order of magnitude longer than the transverse relaxation time. However, to eliminate phonon interactions, ESE-EPR spectroscopy experiments are typically performed at low temperatures. All relaxation times for both color centers

are collected in Table 2, where the dynamic characteristics are comparable to the ensemble values of NV^- centers in diamond [6].

Table 2. Characteristic times of various mechanisms of dephasing of the spin magnetization of color centers.

Vacancy Type	T_1 (ms)	T_2 (μ s)	τ_R (μ s)	Spin-Diffusion	ESEEM Modulation
NV^-	500	50	2.2	No	No
V_B^-	3.52	15	5.5	Yes	Yes

The observation of nuclear modulation is determined by multiple factors, such as the magnitude of the anisotropic dipole–dipole coupling, the degree of the spin Hamiltonian tensors noncollinearity, crystal orientation, etc. The authors suggest that the difference in the strength of the hyperfine coupling, namely the dipole–dipole contribution, can directly affect the reason for the occurrence or absence of nuclear modulations. The presence of the ESEEM modulation effect makes it possible to read out the state of nuclear sublevels utilizing only microwave pulses, without the use of additional radio frequency sources (ENDOR spectroscopy). On the other hand, nuclear modulations can contribute to an additional loss of spin phase coherence of the qubit and, accordingly, reduce the relaxation time T_2 .

3.3. Room Temperature Measurements

Magnetic resonance studies at room temperature are of particular interest because one of the trends in technical development is the transition from helium or nitrogen to ambient conditions. Experiments at room temperature are more convenient in terms of financial costs and personnel due to the avoidance of expensive vacuum and cryogenic installations. The results of ESE-EPR spectroscopy obtained at $Temp. = 297$ K are shown in Figure 4. As a negative result, the absence of spin polarization of the V_B^- in hBN upon excitation by an optical quantum is noted (Figure 4a). At maximum output power, only a slight redistribution of intensity is observed, which affects the skew of the V_B^- fine structure components. Under similar experimental conditions for the NV^- center in SiC, laser excitation leads to effective spin polarization with the formation of “population inversion”. This effect can be used to create masers at room temperature based on color centers. Insufficient optical excitation power and a competing advanced recombination process at $Temp. = 297$ K, i.e., polarization decay, does not allow creating a population inversion for a boron vacancy. The use of more powerful lasers with constant heat removal by Peltier elements to avoid overheating of the crystal will presumably significantly increase the extent of spin polarization.

The relaxation times (T_1 and T_2) of defects at $Temp. = 297$ K (Figure 4b) have undergone significant changes compared to conditions at $Temp. = 10$ K (Figure 3), reduced by several orders of magnitude in the case of T_1 and several times for time T_2 (Table 3). The mechanisms responsible for longitudinal relaxation strongly depend on the temperature (phonon vibration modes) of the crystal, and therefore the time sweep changed from the millisecond to the microsecond region. The T_1 time of a V_B^- is only 20 μ s, which is not enough to conduct ENDOR experiments to analyze the local environment and dipole–dipole or quadrupole interactions. The ENDOR method involves the use of a Mims pulse sequence with the observation of a stimulated ESE, where a RF pulse is used as an additional excitation source. Successful initiation of nuclear magnetic transitions for ^{14}N requires an RF pulse length of 72 to 90 μ s, which is greater than the $3T_1$ value (60 μ s) of a V_B^- where 97% of the spin magnetization is lost. Thus, for a V_B^- at room temperature there is no possibility of implementing ENDOR manipulations, which could find its application in the role of quantum registers based on electronic and nuclear qubits. In the case of NV^- in SiC, a duration of $T_1 = 100$ μ s is sufficient to observe ENDOR signals and thus a readout of the states of ^{14}N nuclear sublevels at room temperature has recently been proposed [36].

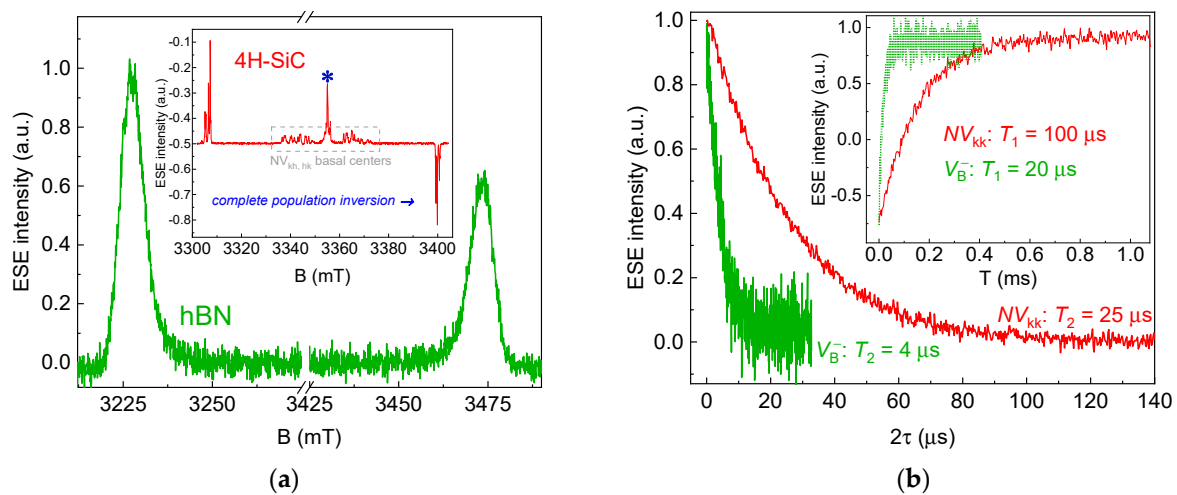


Figure 4. (a) EPR spectra of color centers at $Temp. = 297$ K, where the green solid line is a V_B^- in hBN, the red line in the inset is an NV^- center in SiC. The middle peak marked by a violet asterisk on the inset refers to an interstitial defect with electron spin $S = 1/2$. This spin center is independent of optical excitation of any wavelength (260–980 nm) and is beyond the scope of our study. (b) Spin–spin (T_2) or transverse relaxation and spin–lattice (T_1) or longitudinal relaxation (inset) curves for both color centers, where green is the V_B^- in hBN, red is the NV^- center in SiC.

Table 3. Relaxation times of color centers at room temperature.

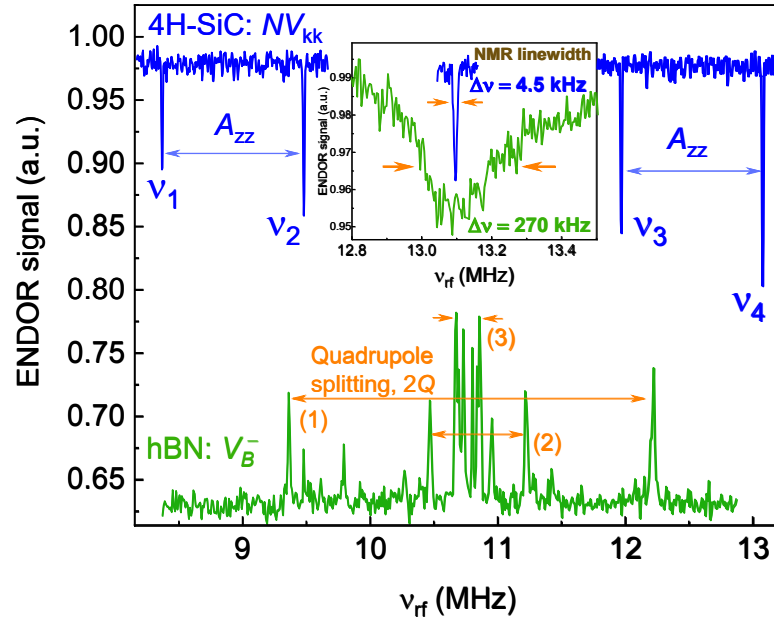
Vacancy Type	T_1 (μ s)	T_2 (μ s)	Spin Polarization	ENDOR Effect
NV^-	100	25	Yes	Yes
V_B^-	20	4	No	No

3.4. Electron–Nuclear Interactions

The presence of a ^{14}N magnetic nucleus vacancy near the electron spin ($I = 1$, 99.69%) both in the case of a V_B^- in hBN and for an NV^- center in SiC allows us to observe additional structures caused by hyperfine and quadrupole interactions, described by the last two components of the spin Hamiltonian. In this work, the ENDOR method makes it possible to register signals of the order of ≈ 1 MHz, which in turn cannot be resolved in the EPR spectrum due to broadening and some important information is lost. Figure 5 shows the ENDOR spectra obtained under the same experimental conditions in the region of the Larmor frequency of ^{14}N nuclei $\nu_L = 10.2$ MHz ($B_0 = 3.4$ T), where the solid line refers to the NV^- center signal, and the green line to the V_B^- . The ENDOR spectrum for the NV^- center contains four narrow lines corresponding to NMR transitions of nitrogen nuclei between hyperfine ($\nu_2 - \nu_1 = \nu_4 - \nu_3 = A_{zz}$) and quadrupole ($\nu_3 - \nu_1 = \nu_4 - \nu_2 = Q$) sublevels splitting. Four NMR transition frequencies ν_{1-4} are defined by the following combinations: $\nu_{1,3} = \nu_L \pm P$ and $\nu_{2,4} = \nu_L - A_{||} \pm P$, where $\nu_L = \gamma_N B_0$ (γ_N —gyromagnetic ratio) ^{14}N nuclear Larmor frequency, $A_{||} = A_{iso} + 2A_{dip-dip}$ is the hyperfine interaction constant, and P is the nuclear quadrupole splitting. These frequencies ν_{1-4} are shown in the top ENDOR spectrum of Figure 5. Among the features, one can note the negative value of the isotropic contribution to the hyperfine interaction, which corresponds to the contact Fermi contribution and is determined by the degree of localization in the electron density of the vacancy on the ^{14}N nucleus. It was explained in refs. [13,36] by the fact that the main part of the electron density of the NV^- center is concentrated on the three nearest carbon atoms, which in turn polarizes the electron core on the ^{14}N nucleus, forming a negative sign. A similarly negative hyperfine value is observed for the NV^- center in diamond ($A_{iso} = -2.47$ MHz) [6]. It is worth noting that the dipole–dipole anisotropic component is small and makes up only a 10 kHz contribution. In the case of an NV^- center, the hyperfine interaction with a value of $A_{zz} = 1.1$ MHz < 10 MHz (Larmor frequency) belongs to the “weak coupling” type [33].

Table 4. Values of the spin Hamiltonian (1) of color centers related to electron–nuclear interactions.

Vacancy Type	A_{iso} (MHz)	$A_{dip-dip}$ (MHz)	C_Q (MHz)	η	Line-Width (kHz)
NV^-	−1.1	0.01	2.53	0	4.5
V_B^-	59.3	13.7	2.11	0.007	270

**Figure 5.** ENDOR spectra for SiC and hBN irradiated crystals. Hyperfine and quadrupole splitting values of the spin Hamiltonian (1) are shown in Table 4. The top inset shows individual NMR absorption lines for ^{14}N nuclei in the hBN and SiC crystal with significantly different line widths $\Delta\nu$.

The boron vacancy is surrounded by three equidistant nitrogen atoms forming an equivalent hyperfine interaction with a structure of seven lines ($2 \times I \times n + 1 = 7$, $I = 1$, n is the number of atoms). In the ENDOR spectrum in Figure 5, observing three pairs of splittings (labeled QI) can be caused by quadrupole interactions (C_Q , quadrupole coupling constant) from each of the three nitrogen atoms when the crystal is oriented perpendicular to B_0 . In the case of a V_B^- , the magnitude of the hyperfine interaction (85 MHz) is greater than the Larmor frequency ^{14}N , which is now referred to as “strong coupling”. The magnitude of the isotropic hyperfine interaction depends on the electron density of the spin defect on the magnetic isotope nucleus as follows: $A_{iso} = \frac{8\pi}{3} g \mu_B g_N \mu_N |\psi_{2s}(0)|^2$, where $\psi_{2s}(0)$ is a wave function amplitude [37]. Theoretical calculations using the approach described in [23] allow establishing the electron density part ($\approx 84\%$) of the V_B^- ($A_{iso} = 59.3$ MHz) as predominantly localized on the three nearest nitrogen nuclei. In this case, the NV^- center has strict axial symmetry with $\approx 1.62\%$ electron density on the neighboring ^{14}N nuclear, and while the V_B^- has a weak orthorhombic distortion in the plane of the layer, it does not reflect a non-zero asymmetry parameter $\eta = 0.007$. The extent of spin density distribution of the color center is critical to the relaxation properties, which can serve as an additional source of phase coherence loss. Strong coupling determines greater sensitivity to local fluctuations due to nuclear spin diffusion. The obtained data on electron–nuclear interactions correlate with the dynamic characteristics from Section 3.2.

As a comparative analysis, the inset shows individual NMR transition lines in parallel orientation for the NV^- center and V_B^- . It is assumed that the main contribution to the width of the ENDOR lines is the scatter in the magnitude of the anisotropic dipole–dipole interaction, which depends on the third power on the electron–nuclear distance: $A_{dip-dip} = \frac{2}{5} g \mu_B g_N \mu_N r^{-3}$. The linewidth for V_B^- is significantly larger (60 times) than for the NV^- center correlating with a difference between the hyperfine interaction values, which may be due to the strong distribution of distances between boron vacancies and

nitrogen atoms (dangling bonds) owing to the two-dimensional nature of the hBN crystal. The ENDOR resonance lines of the NV^- center are extremely narrow and resolved, which allows the highly selective excitations required for point-by-point readout of spin states (qubits) in quantum technologies. The electron–nuclear interaction values listed in Table 4 in the same orders are also presented in well-known scientific papers related to the boron vacancy in hBN [22] crystals, and NV^- centers in diamond [6,38], and silicon carbide [29] crystals.

Electron–nuclear interactions play a significant role in considering color centers as quantum registers, since it becomes possible to create multi-level spin systems and implement complex quantum registers [39]. Optically initialized spin defects with bound magnetic nuclei are an attractive basis for quantum technologies. Spin polarization due to optical excitation makes it possible to organize “spin-photon” interfaces [40], while the transfer of magnetization from the electronic to the nuclear subsystem can solve the issue of long-lived quantum memory [41]. Thus, the presented analysis of hyperfine and quadrupole quantities is of interest for quantum information technologies based on color centers surrounded by nuclear spins.

4. Conclusions

In this work, based on the results of electron paramagnetic resonance and double electron–nuclear resonance methods, a comparative analysis of the spin–optical, electron–nuclear, and relaxation properties of nitrogen-bound vacancy defects is presented. The main quantities of the spin Hamiltonian for each color center, namely the NV^- center in 4H-SiC: $D = 1.3$ GHz, $A_{zz} = 1.1$ MHz, and $C_Q = 2.53$ MHz, as well as for boron vacancy in hBN: $D = 3.6$ GHz, $A_{zz} = 85$ MHz, and $C_Q = 2.11$ MHz, depending on the type of matrix, are analyzed. The spin–spin relaxation times T_2 (NV^- center: 50 μ s and V_B^- : 15 μ s) and their dependence on the local nuclear environment under the influence of nuclear spin diffusion are shown. The Rabi oscillation damping time depends on the size of the crystal and the degree of inhomogeneous distribution of the magnetic component of the microwave excitation. The ENDOR absorption width for color centers differs significantly by more than 60 times due to the structural features of each covalent crystal. The presented results have an applied nature in the importance of choosing a material platform when creating quantum registers based on high-spin color centers for quantum information systems.

Author Contributions: Conceptualization H.J.v.B. and M.G.; methodology G.M. and M.S.; software G.M.; validation L.L., F.M., M.G. and H.J.v.B.; formal analysis F.M. and G.M.; investigation G.M. and M.S.; writing—original draft preparation F.M. and M.G.; writing—review and editing L.L. and H.J.v.B.; project administration F.M.; funding acquisition F.M. All authors have read and agreed to the published version of the manuscript.

Funding: This study was funded by the subsidy allocated to Kazan Federal University for the state assignment in the sphere of scientific activities (Project No. FZSM-2024-0010).

Data Availability Statement: Data can be available upon request from the authors.

Conflicts of Interest: The authors declare no conflicts of interest.

References

1. Gordon, L.; Weber, J.R.; Varley, J.B.; Janotti, A.; Awschalom, D.D.; Van de Walle, C.G. Quantum Computing with Defects. *MRS Bull.* **2013**, *38*, 802–807. [[CrossRef](#)]
2. Weber, J.R.; Koehl, W.F.; Varley, J.B.; Janotti, A.; Buckley, B.B.; Van de Walle, C.G.; Awschalom, D.D. Quantum Computing with Defects. *Proc. Natl. Acad. Sci. USA* **2010**, *107*, 8513–8518. [[CrossRef](#)] [[PubMed](#)]
3. Strikis, A.; Benjamin, S.C.; Brown, B.J. Quantum Computing Is Scalable on a Planar Array of Qubits with Fabrication Defects. *Phys. Rev. Appl.* **2023**, *19*, 064081. [[CrossRef](#)]
4. Gardas, B.; Dziarmaga, J.; Zurek, W.H.; Zwolak, M. Defects in Quantum Computers. *Sci. Rep.* **2018**, *8*, 4539. [[CrossRef](#)] [[PubMed](#)]
5. Wolfowicz, G.; Heremans, F.J.; Anderson, C.P.; Kanai, S.; Seo, H.; Gali, A.; Galli, G.; Awschalom, D.D. Quantum Guidelines for Solid-State Spin Defects. *Nat. Rev. Mater.* **2021**, *6*, 906–925. [[CrossRef](#)]

6. Doherty, M.W.; Manson, N.B.; Delaney, P.; Jelezko, F.; Wrachtrup, J.; Hollenberg, L.C.L. The Nitrogen-Vacancy Colour Centre in Diamond. *Phys. Rep.* **2013**, *528*, 1–45. [[CrossRef](#)]
7. Schirhagl, R.; Chang, K.; Loretz, M.; Degen, C.L. Nitrogen-Vacancy Centers in Diamond: Nanoscale Sensors for Physics and Biology. *Annu. Rev. Phys. Chem.* **2014**, *65*, 83–105. [[CrossRef](#)] [[PubMed](#)]
8. Li, X.-K.; Ma, S.-L.; Ren, Y.-L.; Xie, J.-K.; Li, F.-L. Coupling a Single NV Center to a Superconducting Flux Qubit via a Nanomechanical Resonator. *J. Opt. Soc. Am. B* **2022**, *39*, 69–76. [[CrossRef](#)]
9. Liu, T.; Xu, J.; Zhang, Y.; Yu, Y.; Su, Q.-P.; Zhou, Y.-H.; Yang, C.-P. Efficient Scheme for Implementing a Hybrid Toffoli Gate with Two NV Ensembles Simultaneously Controlling a Single Superconducting Qubit. *Appl. Phys. Lett.* **2023**, *123*, 134002. [[CrossRef](#)]
10. Boixo, S.; Isakov, S.V.; Smelyanskiy, V.N.; Babbush, R.; Ding, N.; Jiang, Z.; Bremner, M.J.; Martinis, J.M.; Neven, H. Characterizing Quantum Supremacy in Near-Term Devices. *Nat. Phys.* **2018**, *14*, 595–600. [[CrossRef](#)]
11. de Leon, N.P.; Itoh, K.M.; Kim, D.; Mehta, K.K.; Northup, T.E.; Paik, H.; Palmer, B.S.; Samarth, N.; Sangtawesin, S.; Steuerman, D.W. Materials Challenges and Opportunities for Quantum Computing Hardware. *Science* **2021**, *372*, eabb2823. [[CrossRef](#)] [[PubMed](#)]
12. Mizuochi, N.; Yamasaki, S.; Takizawa, H.; Morishita, N.; Ohshima, T.; Itoh, H.; Isoya, J. Continuous-Wave and Pulsed EPR Study of the Negatively Charged Silicon Vacancy with $S=3/2$ and C_{3v} Symmetry in n-Type 4H-SiC. *Phys. Rev. B* **2002**, *66*, 235202. [[CrossRef](#)]
13. Baranov, P.G.; Bundakova, A.P.; Soltamova, A.A.; Orlinskii, S.B.; Borovykh, I.V.; Zondervan, R.; Verberk, R.; Schmidt, J. Silicon Vacancy in SiC as a Promising Quantum System for Single-Defect and Single-Photon Spectroscopy. *Phys. Rev. B* **2011**, *83*, 125203. [[CrossRef](#)]
14. Davidsson, J.; Ivády, V.; Armiento, R.; Ohshima, T.; Son, N.T.; Gali, A.; Abrikosov, I.A. Identification of Divacancy and Silicon Vacancy Qubits in 6H-SiC. *Appl. Phys. Lett.* **2019**, *114*, 112107. [[CrossRef](#)]
15. Murzakhanov, F.F.; Sadovnikova, M.A.; Mamin, G.V.; Nagalyuk, S.S.; von Bardeleben, H.J.; Schmidt, W.G.; Biktagirov, T.; Gerstmann, U.; Soltamov, V.A. 14N Hyperfine and Nuclear Interactions of Axial and Basal NV Centers in 4H-SiC: A High Frequency (94 GHz) ENDOR Study. *J. Appl. Phys.* **2023**, *134*, 123906. [[CrossRef](#)]
16. Murzakhanov, F.F.; Yavkin, B.V.; Mamin, G.V.; Orlinskii, S.B.; von Bardeleben, H.J.; Biktagirov, T.; Gerstmann, U.; Soltamov, V.A. Hyperfine and Nuclear Quadrupole Splitting of the NV- Ground State in 4H-SiC. *Phys. Rev. B* **2021**, *103*, 245203. [[CrossRef](#)]
17. Sato, S.; Narahara, T.; Abe, Y.; Hijikata, Y.; Umeda, T.; Ohshima, T. Formation of Nitrogen-Vacancy Centers in 4H-SiC and Their near Infrared Photoluminescence Properties. *J. Appl. Phys.* **2019**, *126*, 083105. [[CrossRef](#)]
18. Lee, S.W.; Vlaskina, S.I.; Vlaskin, V.I.; Zaharchenko, I.V.; Gubanov, V.A.; Mishinova, G.N.; Svechnikov, G.S.; Rodionov, V.E.; Podlasov, S.A. Silicon Carbide Defects and Luminescence Centers in Current Heated 6H-SiC. *Semicond. Phys. Quantum Electron. Optoelectron.* **2010**, *13*, 24. [[CrossRef](#)]
19. Castelletto, S.; Boretti, A. Silicon Carbide Color Centers for Quantum Applications. *J. Phys. Photonics* **2020**, *2*, 022001. [[CrossRef](#)]
20. Liu, X.; Hersam, M.C. 2D Materials for Quantum Information Science. *Nat. Rev. Mater.* **2019**, *4*, 669–684. [[CrossRef](#)]
21. Roy, S.; Zhang, X.; Puthirath, A.B.; Meiyazhagan, A.; Bhattacharyya, S.; Rahman, M.M.; Babu, G.; Susarla, S.; Saju, S.K.; Tran, M.K.; et al. Structure, Properties and Applications of Two-Dimensional Hexagonal Boron Nitride. *Adv. Mater.* **2021**, *33*, 2101589. [[CrossRef](#)] [[PubMed](#)]
22. Gottscholl, A.; Kianinia, M.; Soltamov, V.; Orlinskii, S.; Mamin, G.; Bradac, C.; Kasper, C.; Krambrock, K.; Sperlich, A.; Toth, M.; et al. Initialization and Read-out of Intrinsic Spin Defects in a van Der Waals Crystal at Room Temperature. *Nat. Mater.* **2020**, *19*, 540–545. [[CrossRef](#)] [[PubMed](#)]
23. Shaik, A.B.D.; Palla, P. Optical Quantum Technologies with Hexagonal Boron Nitride Single Photon Sources. *Sci. Rep.* **2021**, *11*, 12285. [[CrossRef](#)] [[PubMed](#)]
24. Gottscholl, A.; Diez, M.; Soltamov, V.; Kasper, C.; Krauß, D.; Sperlich, A.; Kianinia, M.; Bradac, C.; Aharonovich, I.; Dyakonov, V. Spin Defects in hBN as Promising Temperature, Pressure and Magnetic Field Quantum Sensors. *Nat. Commun.* **2021**, *12*, 4480. [[CrossRef](#)] [[PubMed](#)]
25. Gracheva, I.N.; Murzakhanov, F.F.; Mamin, G.V.; Sadovnikova, M.A.; Gabbasov, B.F.; Mokhov, E.N.; Gafurov, M.R. Symmetry of the Hyperfine and Quadrupole Interactions of Boron Vacancies in a Hexagonal Boron Nitride. *J. Phys. Chem. C* **2023**, *127*, 3634–3639. [[CrossRef](#)]
26. Kianinia, M.; White, S.; Fröch, J.E.; Bradac, C.; Aharonovich, I. Generation of Spin Defects in Hexagonal Boron Nitride. *ACS Photonics* **2020**, *7*, 2147–2152. [[CrossRef](#)]
27. Gao, X.; Pandey, S.; Kianinia, M.; Ahn, J.; Ju, P.; Aharonovich, I.; Shivaram, N.; Li, T. Femtosecond Laser Writing of Spin Defects in Hexagonal Boron Nitride. *ACS Photonics* **2021**, *8*, 994–1000. [[CrossRef](#)]
28. Gerstmann, U.; Rauls, E.; Frauenheim, T.; Overhof, H. Formation and Annealing of Nitrogen-Related Complexes in SiC. *Phys. Rev. B* **2003**, *67*, 205202. [[CrossRef](#)]
29. von Bardeleben, H.J.; Cantin, J.L.; Rauls, E.; Gerstmann, U. Identification and Magneto-Optical Properties of the NV Center in 4H-SiC. *Phys. Rev. B* **2015**, *92*, 064104. [[CrossRef](#)]
30. Liu, W.; Guo, N.-J.; Yu, S.; Meng, Y.; Li, Z.-P.; Yang, Y.-Z.; Wang, Z.-A.; Zeng, X.-D.; Xie, L.-K.; Li, Q.; et al. Spin-Active Defects in Hexagonal Boron Nitride. *Mater. Quantum. Technol.* **2022**, *2*, 032002. [[CrossRef](#)]
31. Strand, J.; Larcher, L.; Shluger, A.L. Properties of Intrinsic Point Defects and Dimers in Hexagonal Boron Nitride. *J. Phys. Condens. Matter* **2019**, *32*, 055706. [[CrossRef](#)] [[PubMed](#)]

32. Berliner, L.J.; Eaton, S.S.; Eaton, G.R. *Distance Measurements in Biological Systems by EPR*; Springer Science & Business Media: Berlin/Heidelberg, Germany, 2006.
33. Goldfarb, D.; Stoll, S. *EPR Spectroscopy: Fundamentals and Methods*; John Wiley & Sons: Hoboken, NJ, USA, 2018.
34. Ye, M.; Seo, H.; Galli, G. Spin Coherence in Two-Dimensional Materials. *npj Comput. Mater.* **2019**, *5*, 44. [[CrossRef](#)]
35. Baibekov, E.I. Decay of Rabi Oscillations Induced by Magnetic Dipole Interactions in Dilute Paramagnetic Solids. *JETP Lett.* **2011**, *93*, 292–297. [[CrossRef](#)]
36. Murzakhonov, F.; Sadovnikova, M.; Mamin, G.; Sannikov, K.; Shakirov, A.; von Bardeleben, H.J.; Mokhov, E.; Nagalyuk, S. Room Temperature Coherence Properties and ¹⁴N Nuclear Spin Readout of NV Centers in 4H–SiC. *Appl. Phys. Lett.* **2024**, *124*, 034001. [[CrossRef](#)]
37. Kaupp, M.; Bühl, M.; Malkin, V.G. Introduction: The Quantum Chemical Calculation of NMR and EPR Parameters. In *Calculation of NMR and EPR Parameters*; John Wiley & Sons, Ltd.: Hoboken, NJ, USA, 2004; pp. 1–5. [[CrossRef](#)]
38. Felton, S.; Edmonds, A.M.; Newton, M.E.; Martineau, P.M.; Fisher, D.; Twitchen, D.J.; Baker, J.M. Hyperfine Interaction in the Ground State of the Negatively Charged Nitrogen Vacancy Center in Diamond. *Phys. Rev. B* **2009**, *79*, 075203. [[CrossRef](#)]
39. Takou, E.; Barnes, E.; Economou, S.E. Precise Control of Entanglement in Multinuclear Spin Registers Coupled to Defects. *Phys. Rev. X* **2023**, *13*, 011004. [[CrossRef](#)]
40. Xiong, Y.; Bourgois, C.; Sheremetyeva, N.; Chen, W.; Dahliah, D.; Song, H.; Zheng, J.; Griffin, S.M.; Sipahigil, A.; Hautier, G. High-Throughput Identification of Spin-Photon Interfaces in Silicon. *Sci. Adv.* **2023**, *9*, eadh8617. [[CrossRef](#)] [[PubMed](#)]
41. Fuchs, G.D.; Burkard, G.; Klimov, P.V.; Awschalom, D.D. A Quantum Memory Intrinsic to Single Nitrogen–Vacancy Centres in Diamond. *Nature Phys.* **2011**, *7*, 789–793. [[CrossRef](#)]

Disclaimer/Publisher’s Note: The statements, opinions and data contained in all publications are solely those of the individual author(s) and contributor(s) and not of MDPI and/or the editor(s). MDPI and/or the editor(s) disclaim responsibility for any injury to people or property resulting from any ideas, methods, instructions or products referred to in the content.